PDEBENCH: AN EXTENSIVE BENCHMARK FOR SCIENTIFIC MACHINE LEARNING.
SUPPLEMENTARY MATERIAL

A RELATED WORK

PDE benchmarking has particular challenges. Unlike many classic datasets, PDE datasets can be large on a gigabyte or terabyte scale and still contain only few data points. And unlike monolithic benchmark datasets such as ImageNet, the datasets for each PDE approximation task are specific to that task. Each set of governing equations or experiment design assumptions leads to a distinct dataset of PDE samples. Recent works in PDEs have attempted to produce standardised datasets covering well-known challenges (Otness et al., 2021; Huang et al., 2021; Stachenfeld et al., 2022). Huang et al. (2021) targets non-ML uses. Stachenfeld et al. (2022) is specialised for particular classes of equations. Of these, the excellent work of Otness et al. (2021) is most closely related, but with only four physical systems, it still lacks sufficient scale and diversity of data to challenge emerging ML algorithms. We expand the range of benchmarks in this domain by providing a larger, more diverse problem selection and scale than these previous attempts (11 PDEs with different parametrizations leading to 35 datasets). We additionally consider inverse problems for PDEs (Stuart, 2010; Tarantola, 2005), with the goal to identify unobserved latent parameters using ML. This has not been covered by benchmarks so far, despite its increasing importance in the community. Furthermore, most work in this scope considers classical statistical error measures such as the RMSE over the whole domain and at most PDE-motivated variants such as the RMSE of the gradient Otness et al. (2021). Measures based on properties of the underlying physical systems, as studied in this work, are lacking.

An overview and taxonomy of Scientific ML developments can be found in Lavin et al. (2021); Brunton & Kutz (2019). For developing our baselines, we focus on using neural network models to approximate the outputs of some *ground truth* PDE solver, given data generated by that solver, which itself aims to directly implement the numerical solution of a given partial differential equation. A range of methods aim to solve problems fitting this description, reviewed in Kashinath et al. (2021). Methods include Physics-informed neural networks (PINNs) (Raissi et al., 2019), Neural operators (NOs) (Li et al., 2021; Kovachki et al., 2021), treating ResNet as a PDE approximant (Ruthotto & Haber, 2018), custom architectures for specific problems such as TFNet for turbulent fluid flows (Wang et al., 2020), and generic image-to-image regression models such as the U-Net (Ronneberger et al., 2015). These approaches each have different assumptions, domains of applicability, and data processing requirements.

Benchmarks in machine learning are an ubiquitous feature of the field. In recent years, their design and implementation has become a research area of its own right. Easily accessible and widely used image classification benchmarks such as MNIST, CIFAR, and ImageNet are widely credited with accelerating progress in machine learning. Various domains in machine learning have widely influential datasets: In time series forecasting there are the Makridakis competitions (Makridakis et al., 2020), in reinforcement learning there is the OpenAI Gym (Brockman et al., 2016). Generic classification problems use, for example, the Penn Machine Learning Benchmark (Olson et al., 2017).

Closely related to the chosen Scientific ML baselines is the problem of directly differentiating through the numerical solver, which can itself be used in training an approximating model, or to directly solve some optimization or control problem of interest. Differentiable direct PDE solvers are increasingly available, e.g. Mitusch et al. (2019) and frequently built upon neural network technology stacks (Freeman et al., 2021; Bezgin et al., 2022; Holl & Koltun, 2020).

Recent efforts have attempted to unify Scientific ML surrogates for PDEs under a single interface. For example, NVIDIA's MODULUS/SimNet (Hennigh et al., 2020) implements a variety of methods in a single framework, although unfortunately under onerous intellectual property restrictions and an opaque contribution process. The DeepXDE project (Lu et al., 2021) is available under an open license and provides an impressive range of capabilities, but is largely restricted to PINN and DeepONet methods (Raissi et al., 2019).

B DETAILED METRICS DESCRIPTION

The classic loss metrics we use are (1) root-mean-squared-error (RMSE), (2) normalized RMSE (nRMSE), (3) maximum error. These measure the emulating model's global performance but neglect local performance. Thus we include extra metrics to measure specific failure modes: (4) RMSE of the conserved value (cRMSE), (5) RMSE at boundaries (bRMSE), (6) RMSE in Fourier space (fRMSE) constrained to low, middle, and high-frequency regions.

The normalized RMSE is a variant of the RMSE to provide scale-independent information defined as:

$$\mathrm{nRMSE} \equiv \sqrt{\frac{||u_{\mathrm{pred}} - u_{\mathrm{true}}||_2}{||u_{\mathrm{true}}||_2}}, \tag{1}$$

where $||u||_2$ is the L_2-norm of a (vector-valued) variable u, and $u_{\mathrm{true}}, u_{\mathrm{pred}}$ are true and predicted value, respectively. The maximum error measures the model's worst prediction, which quantifies both local performance and models' stability of their prediction. cRMSE is defined as $\mathrm{nRMSE} \equiv ||\sum u_{\mathrm{pred}} - \sum u_{\mathrm{true}}||_2/N$, which measure the deviation of the prediction from some physically conserved value. bRMSE measures the error at the boundary, indicating if the model understand the boundary condition properly. Finally, fRMSE measures the error in low/middle/high-frequency ranges defined as

$$\frac{\sqrt{\sum_{k_{\mathrm{min}}}^{k_{\mathrm{max}}} |\mathcal{F}(u_{\mathrm{pred}}) - \mathcal{F}(u_{\mathrm{true}}))|^2}}{k_{\mathrm{max}} - k_{\mathrm{min}} + 1}, \tag{2}$$

where $\mathcal{F}$ is a discrete Fourier transformation, and k_{min}, k_{max} are the minimum and maximum indices in Fourier coordinates. In our paper, we define the low/middle/high-frequency regions as Low: $k_{\mathrm{min}} = 0, k_{\mathrm{max}} = 4$, Middle: $k_{\mathrm{min}} = 5, k_{\mathrm{max}} = 12$, and High: $k_{\mathrm{min}} = 13, k_{\mathrm{max}} = \infty$. This allows a quantitative discussion of the model performance's dependence on the wavelength. In the multi-dimensional cases, we first integrate the angular coordinate direction of $|\mathcal{F}[u_{\mathrm{pred}} - u_{\mathrm{true}}](k)|^2$, and take the sum along the k-coordinate.

B.1 INVERSE PROBLEM METRICS

For the inverse problem setup, we selected various metrics. The major difference with respect to the forward metrics is that we have two main quantities to measure:

- the error of the *quantity* we want to estimate, in our case the initial condition u_0:

  $$\mathcal{L}(u_0, \hat{u}_0)$$

  where $\hat{u}_0$ is the estimated value;
- the error of the *prediction* based on the estimated initial condition $u(t, x|u_0)$,

  $$\mathcal{L}\left(u(t, x|u_0), u(t, x|\hat{u}_0)\right)$$

In general, we expect a larger error when we measure the error in the estimated quantity w.r.t. the predicted quantity. This is mainly due to the early decay of high frequencies of the PDE. We evaluated the error of the prediction at a specific instant in time $t = T$, that has been selected as $T = 15$ for all the tested datasets, expect $T = 5$ for the CFD dataset.

The metrics that we used for the inverse problem are: 1) MSE 2) the normalized ℓ_2 norm (L2), 3) the normalized ℓ_3 norm (L3); 4) the FFT MSE, the FFT L2 and 5) the FFT L3. For the frequency metrics we investigated the low frequency (between 0 and $1/4$ of the max frequency), the middle frequency (between $1/4$ and $3/4$) and high frequency (between $3/4$ and the maximum frequency) ranges. In Fig.9, the right figure shows the frequency power density, where we see that the largest error is found in the middle frequency range.

C TRAINING PROTOCOL AND HYPERPARAMETERS

The model was trained for 500 epochs with the Adam optimizer (Kingma & Ba, 2014) as per the protocol of the original FNO. The initial learning rate was set as 10^{-3} and reduced by half after each

100 epochs. The datasets are split into 90% training and 10% validation and testing. For the PINNs, we use DeepXDE (Lu et al., 2021) implementation. The training was performed for 15,000 epochs with the Adam optimizer, with the learning rate set to 10^{-3}. As with the example problems from that library we use a fully-connected network of depth 6 with 40 neurons each. In contrast to the other surrogate models, the PINN baseline can be trained and tested only on a single sample, and is valid only for a specific initial and boundary condition. To get more reliable error bounds, we thus chose to train the PINN baseline for 10 different samples per dataset and average the resulting error metrics.

C.1 Inverse problem

For testing the power of surrogate models to solve inverse problems, we consider a simplified scenario where the machine learning model directly predicts a specific time in the future $t = T$. When training to predict a specific time in the future, we reduce the training time and avoid to consider the effect of training approaches (as discussed in the temporal analysis section **??**) in evaluating the surrogate models. We trained over $N_{\text{epoch}} = 20$ epochs and we selected as final time step $T = 15$ for all tested datasets, expect for the CFD dataset where we selected $T = 5$. We used similar parameters used in the forward training, while we selected 64 hidden values to be estimated for the initial condition and 100 samples to test and 0.2 as learning rate for the gradient method. The loss function for the gradient computation is the MSE.

D Detailed Problem Description

In this section, we provide more detailed descriptions of each PDE and its applications. Note that PDE is the basic mathematical tool to describe the evolution of the system in physics. Interested readers are referred to representative textbooks of physics, for example, (Feynman, 1963).

D.1 1D Advection Equation

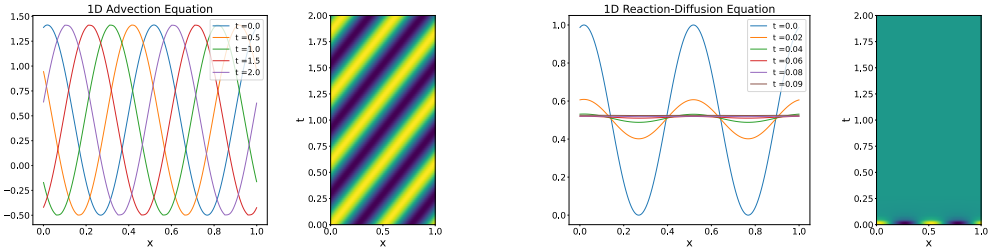

1D Advection ($\beta = 0.4$) 1D Reaction-Diffusion ($\nu = 0.5, \rho = 1$)

Figure 3: Visualization of the time evolution of 1D Advection equation and Reaction-Diffusion equation.

The advection equation models pure advection behavior without non-linearity whose expression is given as:

$$\partial_t u(t,x) + \beta \partial_x u(t,x) = 0, \quad x \in (0,1), t \in (0,2], \tag{3}$$

$$u(0,x) = u_0(x), \; x \in (0,1), \tag{4}$$

where β is a constant advection speed. Note that the exact solution of the system is given as: $u(t,x) = u_0(x - \beta t)$.

In our dataset, we only considered the periodic boundary condition. As an initial condition, we use a super-position of sinusoidal waves as:

$$u_0(x) = \sum_{k_i = k_1, \ldots, k_N} A_i \sin(k_i x + \phi_i), \tag{5}$$

where $k_i = 2\pi\{n_i\}/L_x$ are wave numbers whose $\{n_i\}$ are integer numbers selected randomly in $[1, n_{\max}]$, N is the integer determining how many waves to be added, L_x is the calculation domain

size, A_i is a random float number uniformly chosen in $[0, 1]$, and ϕ_i is the randomly chosen phase in $(0, 2\pi)$. In 1D-advection case, we set $k_{\max} = 8$ and $N = 2$. After calculating Equation 5, we randomly operate the absolute value function with random signature and the window-function with 10% probability, respectively.

The numerical solution was calculated with the temporally and spatially 2nd-order upwind finite difference scheme.

D.2 1D Diffusion-Reaction Equation

Here, we consider a one-dimensional diffusion-reaction type PDE, that combines a diffusion process and a rapid evolution from a source term Krishnapriyan et al. (2021). The equation is expressed as:

$$\partial_t u(t, x) - \nu \partial_{xx} u(t, x) - \rho u(1 - u) = 0, \quad x \in (0, 1), t \in (0, 1], \tag{6}$$

$$u(0, x) = u_0(x), \quad x \in (0, 1). \tag{7}$$

Note that the variable u develops at potentially exponential rate because of the force term which depends on u. measure the ability to capture very rapid dynamics.

Similar to the 1D advection equation case, we use the periodic boundary condition and Equation 5 as the initial condition. To avoid an ill-defined initial condition, we also applied the absolute value function and a normalization operation, dividing the initial condition by the maximum value. The numerical solution was calculated with the temporally and spatially 2nd-order central difference scheme. For the source term part, we use the piecewise-exact solution (PES) method (Inoue et al., 2007).

D.3 Burgers Equation

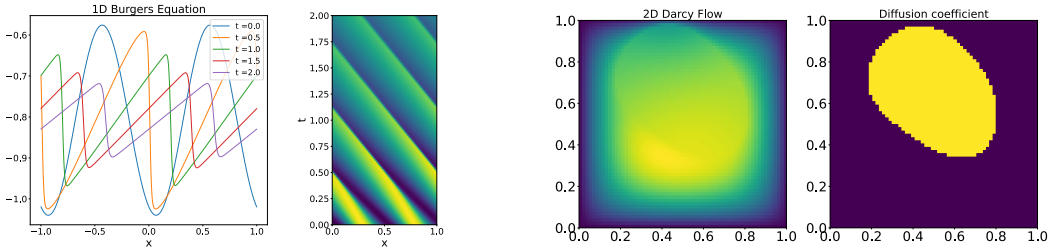

1D Burgers ($\nu = 0.01$) 2D Darcy Flow ($\beta = 1.0$)

Figure 4: Visualization of the time evolution of 1D Burgers equation and 2D Darcy Flow.

The Burgers' equation is a PDE modeling the non-linear behavior and diffusion process in fluid dynamics as

$$\partial_t u(t, x) + \partial_x (u^2(t, x)/2) = \nu/\pi \partial_{xx} u(t, x), \quad x \in (0, 1), t \in (0, 2], \tag{8}$$

$$u(0, x) = u_0(x), \ x \in (0, 1), \tag{9}$$

where ν is the diffusion coefficient, which is assumed constant in our dataset.

Note that setting $R \equiv \pi u L/\nu$ describes the system's evolution as the Reynolds number of the Navier-Stokes equation equation **??**; $R > 1$ means the strong non-linear case support forming shock phenomena, and $R < 1$ means the diffusive case.

Similar to the 1D advection equation case, we use the periodic boundary condition and Equation 5 as the initial condition. The numerical solution was calculated with the temporally and spatially 2nd-order upwind difference scheme for the advection term, and the central difference scheme for the diffusion term.

D.4 Darcy Flow

We experiment with the steady-state solution of 2D Darcy Flow over the unit square, whose viscosity term $a(x)$ is an input of the system. The solution of the steady-state is defined by the following

equation

$$-\nabla(a(x)\nabla u(x)) = f(x), \quad x \in (0,1)^2, \tag{10}$$

$$u(x) = 0, \quad x \in \partial(0,1)^2. \tag{11}$$

In this paper, the force term f is set as a constant value β, changing the scale of the solution $u(x)$. Instead of directly solving Equation 10, we obtained the solution by solving a temporal evolution equation:

$$\partial_t u(x,t) - \nabla(a(x)\nabla u(x,t)) = f(x), \quad x \in (0,1)^2, \tag{12}$$

with random field initial condition, until reaching a steady state. The numerical calculation was performed the same as the case of the 1D Diffusion-Reaction equation.

D.5 Compressible Navier-Stokes equation

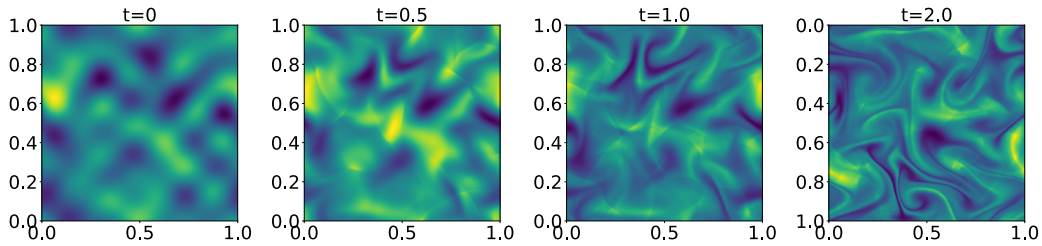

Figure 5: Visualization of the time evolution of the density in the case of 2D Compressible Navier-Stokes equations (inviscid, $M = 0.1$).

The compressible fluid dynamic equations describe a fluid flow,

$$\partial_t \rho + \nabla \cdot (\rho \mathbf{v}) = 0, \tag{13a}$$

$$\rho(\partial_t \mathbf{v} + \mathbf{v} \cdot \nabla \mathbf{v}) = -\nabla p + \eta \triangle \mathbf{v} + (\zeta + \eta/3)\nabla(\nabla \cdot \mathbf{v}), \tag{13b}$$

$$\partial_t \left[\epsilon + \frac{\rho v^2}{2}\right] + \nabla \cdot \left[\left(\epsilon + p + \frac{\rho v^2}{2}\right)\mathbf{v} - \mathbf{v} \cdot \sigma'\right] = 0, \tag{13c}$$

where ρ is the mass density, $\mathbf{v}$ is the velocity, p is the gas pressure, $\epsilon = p/(\Gamma - 1)$ is the internal energy, $\Gamma = 5/3$, σ' is the viscous stress tensor, and η, ζ are the shear and bulk viscosity, respectively.

PDEBench provides the following training datasets for the compressible Navier-Stokes equations:

N_d	initial field	boundary condition	(η, ζ, M)
1D	random field	periodic	$(10^{-8}, 10^{-8}, -)$
1D	random field	periodic	$(10^{-2}, 10^{-2}, -)$
1D	random field	periodic	$(10^{-1}, 10^{-1}, -)$
1D	random field	out-going	$(10^{-8}, 10^{-8}, -)$
1D	shock-tube	out-going	$(10^{-8}, 10^{-8}, -)$
2D	random field	periodic	$(10^{-8}, 10^{-8}, 0.1)$
2D	random field	periodic	$(10^{-2}, 10^{-2}, 0.1)$
2D	random field	periodic	$(10^{-1}, 10^{-1}, 0.1)$
2D	random field	periodic	$(10^{-8}, 10^{-8}, 1.0)$
2D	random field	periodic	$(10^{-2}, 10^{-2}, 1.0)$
2D	random field	periodic	$(10^{-1}, 10^{-1}, 1.0)$
2D	turbulence	periodic	$(10^{-8}, 10^{-8}, 0.1)$
2D	turbulence	periodic	$(10^{-8}, 10^{-8}, 1.0)$
3D	random field	periodic	$(10^{-8}, 10^{-8}, 1.0)$
3D	random field	periodic	$(10^{-2}, 10^{-2}, 1.0)$

where N_d is the number of spatial dimensions, $M = |v|/c_s$ is the Mach number, $c_s = \sqrt{\Gamma p/\rho}$ is the sound velocity. The outgoing boundary condition is copying the neighbor cell to the boundary region which allows waves and fluid to escape from the computational domain, and is popular for astrohydrodynamics simulations (Stone & Norman, 1992). The random field initial condition is applying Equation 5 which is extended to higher dimensions for the 2D and 3D cases. Note that density and pressure are prepared by adding a uniform background to the perturbation field Equation 5. The turbulence initial condition considers turbulent velocity with uniform mass density and pressure. The velocity is calculated similarly to Equation 5 as

$$\mathbf{v}(x, t = 0) = \sum_{i=1}^{n} \mathbf{A}_i \sin(k_i x + \phi_i), \tag{14}$$

where $n = 4$ and $A_i = \bar{v}/|k|^d$, and $d = 1, 2$ when considering 2D and 3D, respectively. $\bar{v}$ is determined by the initial Mach number as $\bar{v} = c_s M$. To reduce the compressibility effect, we subtracted the compressible field from Equation 14 by the Helmholtz-decomposition in the Fourier space.

The shock-tube initial field is composed as $Q(x, t = 0) = (Q_L, Q_R)$, where $Q = (\rho, \mathbf{v}, p)$ and Q_L, Q_R are randomly determined constant values. The location of the initial discontinuity is also randomly determined. This problem is called the "Riemann problem", and the initial discontinuity generates shocks and rarefaction depending on the values of Q_L, Q_R, which are very difficult to obtain without solving the PDEs. This scenario can be used for a rigorous test if ML models fully understand Equation 13a - Equation 13c. The numerical solution was calculated with the temporally and spatially 2nd-order HLLC scheme (Toro et al., 1994) with the MUSCL method (van Leer, 1979) for the inviscid part, and the central difference scheme for the viscous part.

D.6 Inhomogenous, incompressible Navier-Stokes

A popular simplification of the Navier-Stokes equation is the incompressible version, commonly used to model dynamics supposed to be far lower than the speed of propagation of waves in the medium,

$$\nabla \cdot \mathbf{v} = 0, \quad \rho(\partial_t \mathbf{v} + \mathbf{v} \cdot \nabla \mathbf{v}) = -\nabla p + \eta \triangle \mathbf{v}. \tag{15}$$

These simplify the compressible Navier-Stokes equations Eq. equation **??**, by substituting the first term in Eq. equation 15 instead of the first term in equation 13, from which we can eliminate several elements in the second terms of Eq. equation 15. Additionally, we have introduced the assumption that the fluid is homogeneous (i.e. not a fluid comprising two or more substances of different density or viscosity).

We employ an augmented form of equation 15 which includes a vector field *forcing* term $\mathbf{u}$,

$$\rho(\partial_t \mathbf{v} + \mathbf{v} \cdot \nabla \mathbf{v}) = -\nabla p + \eta \triangle \mathbf{v} + \mathbf{u}. \tag{16}$$

Non-periodic conditions are included to challenge models which perform well upon periodic domains, such as the FNO (Li et al., 2021). The forcing term poses challenges based upon spatially heterogeneous dynamics. Firstly, this allows us to see if the prediction methods can successfully learn to predict in the presence of heterogeneity. Secondly, this permits us to use the spatially varying random field as a target for inverse inference.

Initial conditions $\mathbf{v}_0$ and inhomogeneous forcing parameters $\mathbf{u}$ are each drawn from isotropic Gaussian random fields with truncated power-law decay τ of the power spectral density and scale σ, where $\tau_{\mathbf{v}_0} = -3, \sigma_{\mathbf{v}_0} = 0.15, \tau_{\mathbf{u}} = -1, \sigma_{\mathbf{u}} = 0.4$. The variation in the resulting field is due to the alteration in the random seed. We set the domain to the unit square $\Omega = [0, 1]^2$, the viscosity to $\nu = 0.01$. Simulations are implemented using Phiflow Holl & Koltun (2020). Boundary conditions are Dirichlet, clamping field velocity to null at the perimeter.

D.7 2D Shallow-Water Equations

The shallow-water equations, derived from the general Navier-Stokes equations, present a suitable framework for modelling free-surface flow problems. In 2D, these come in the form of the following

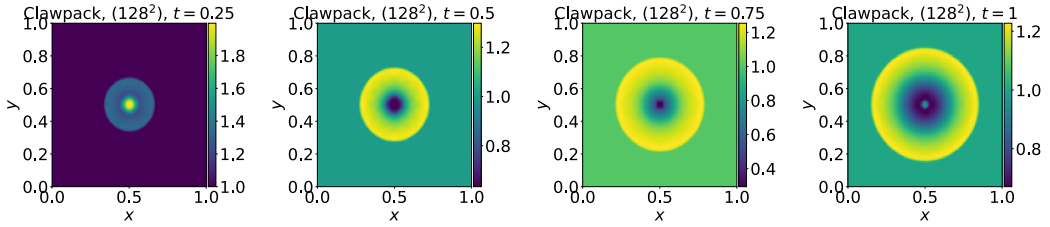

Figure 6: Visualization of the time evolution of the 2D shallow-water equations data.

system of hyperbolic PDEs,

$$\partial_t h + \partial_x hu + \partial_y hv = 0\,, \tag{17a}$$

$$\partial_t hu + \partial_x \left(u^2 h + \frac{1}{2} g_r h^2 \right) + \partial_y uvh = -g_r h \partial_x b\,, \tag{17b}$$

$$\partial_t hv + \partial_y \left(v^2 h + \frac{1}{2} g_r h^2 \right) + \partial_x uvh = -g_r h \partial_y b\,, \tag{17c}$$

with u, v being the velocities in horizontal and vertical direction, h describing the water depth and b describing a spatially varying bathymetry. hu, hv can be interpreted as the directional momentum components and g_r describes the gravitational acceleration.

The specific simulation we include in our benchmark for the shallow-water equations problem as introduced in D.7 is a 2D radial dam break scenario. On a square domain $\Omega = [-2.5, 2.5]^2$ we initialize the water height as a circular bump in the center of the domain

$$h(t = 0, x, y) = \begin{cases} 2.0, & \text{for } r < \sqrt{x^2 + y^2} \\ 1.0, & \text{for } r \geq \sqrt{x^2 + y^2} \end{cases} \tag{18}$$

with the radius r randomly sampled from $\mathcal{U}(0.3, 0.7)$. For generating the datasets we simulate this problem using the PyClaw Ketcheson et al. (2012) Python package which offers a comprehensive finite volume solver. A time evolution visualization of the equation is shown in Figure 6.

D.8 Diffusion-Sorption Equation

The diffusion-sorption equation models a diffusion process which is retarded by a sorption process. The equation is written as

$$\partial_t u(t, x) = D/R(u) \partial_{xx} u(t, x), \quad x \in (0, 1), t \in (0, 500]. \tag{19}$$

where D is the effective diffusion coefficient, R is the retardation factor representing the sorption that hinders the diffusion process. Note that R is dependent on the variable u. This equation is applicable to real world scenarios, one of the most prominent being groundwater contaminant transport.

This equation is retarded by the retardation factor R which is dependent on u based on the Freundlich sorption isotherm Limousin et al. (2007):

$$R(u) = 1 + \frac{1 - \phi}{\phi} \rho_s k n_f u^{n_f - 1}, \tag{20}$$

where $\phi = 0.29$ is the porosity of the porous medium, $\rho_s = 2\,880$ is the bulk density, $k = 3.5 \times 10^{-4}$ is the Freundlich's parameter, $n_f = 0.874$ is the Freundlich's exponent, and the effective diffusion coefficient $D = 5 \times 10^{-4}$. The initial condition is generated with a uniform distribution $u(0, x) \sim \mathcal{U}(0, 0.2)$ for $x \in (0, 1)$. We provide datasets discretized into $N_x = 1024$ and $N_t = 501$, as well as the temporally downsampled version for the models training with $N_t = 101$. The spatial discretization is performed using the finite volume method Moukalled et al. (2016) and the time integration using the built-in fourth order Runge-Kutta method in the *scipy* package Virtanen et al. (2020).

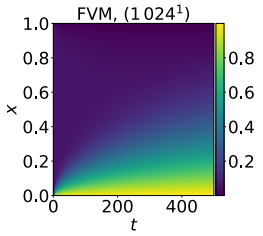

Figure 7: Visualization of the time evolution of the 1D diffusion-sorption equations data.

This particular example is interesting because of a few things. First, the diffusion coefficient becomes non-linear with dependency on u. And based on Equation 20, it is clear that there is a singularity when $u = 0$. Second, it is highly applicable to a real-world problem, namely the groundwater contaminant transport Nowak & Guthke (2016). To date, application of machine learning to real-world physics problems is still rare. Third, we employ boundary conditions that are not the usual zero or periodic conditions that can be easily padded in models with a convolutional structure. Here, we use $u(t, 0) = 1.0$ and $u(t, 1) = D\partial_x u(t, 1)$. The second boundary condition is particularly challenging since it uses a derivative instead of a constant value. For generating the datasets we simulate this problem using a standard finite volume solver. A time evolution visualization of the equation is shown in Figure 7.

D.9 2D Diffusion-Reaction Equation

In addition to the 1D diffusion-reaction equation, which involves only a single variable, we also consider extending the application to a 2D domain, with two non-linearly coupled variables, namely the activator $u = u(t, x, y)$ and the inhibitor $v = v(t, x, y)$. The equation is written as

$$\partial_t u = D_u \partial_{xx} u + D_u \partial_{yy} u + R_u, \quad \partial_t v = D_v \partial_{xx} v + D_v \partial_{yy} v + R_v \,, \tag{21}$$

where D_u and D_v are the diffusion coefficient for the activator and inhibitor, respectively, $R_u = R_u(u, v)$ and $R_v = R_v(u, v)$ are the activator and inhibitor reaction function, respectively. The domain of the simulation includes $x \in (-1, 1), y \in (-1, 1), t \in (0, 5]$. This equation is applicable most prominently for modeling biological pattern formation.

The reaction functions for the activator and inhibitor are defined by the Fitzhugh-Nagumo equation Klaasen & Troy (1984), written as:

$$R_u(u, v) = u - u^3 - k - v, \tag{22}$$
$$R_v(u, v) = u - v, \tag{23}$$

where $k = 5 \times 10^{-3}$, and the diffusion coefficients for the activator and inhibitor are $D_u = 1 \times 10^{-3}$ and $D_v = 5 \times 10^{-3}$, respectively. The initial condition is generated as standard normal random noise $u(0, x, y) \sim \mathcal{N}(0, 1.0)$ for $x \in (-1, 1)$ and $y \in (-1, 1)$. We provide datasets discretized into $N_x = 512$, $N_y = 512$ and $N_t = 501$, as well as the downsampled version for the models training with $N_x = 128$, $N_y = 128$, and $N_t = 101$. As in the 1D diffusion-sorption equation, the spatial discretization is performed using the finite volume method Moukalled et al. (2016), and the time integration is performed using the built-in fourth order Runge-Kutta method in the *scipy* package Virtanen et al. (2020).

We included the 2D diffusion-reaction equation as an example because it serves as a challenging benchmark problem. First, there are two variables of interest, namely the activator and inhibitor, which are non-linearly coupled. Second, it also has applicability in real-world problems, namely biological pattern formation Turing (1952). Third, we also employ a no-flow Neumann boundary condition, meaning that $D_u \partial_x u = 0$, $D_v \partial_x v = 0$, $D_u \partial_y u = 0$, and $D_v \partial_y v = 0$ for $x, y \in (-1, 1)^2$. For generating the datasets we simulate this problem using a standard finite volume solver. A time evolution visualization of the equation is shown in Figure 8.

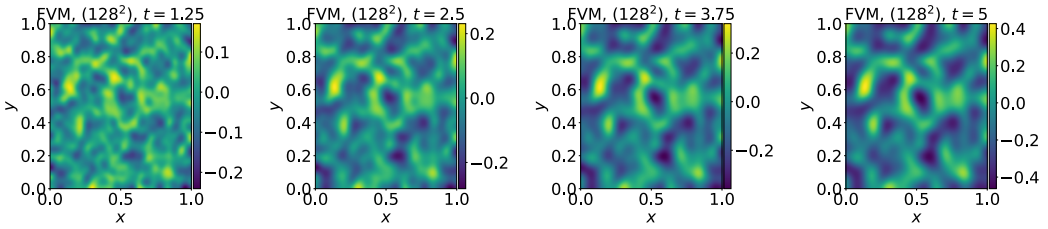

Figure 8: Visualization of the time evolution of the 2D diffusion-reaction equations data.

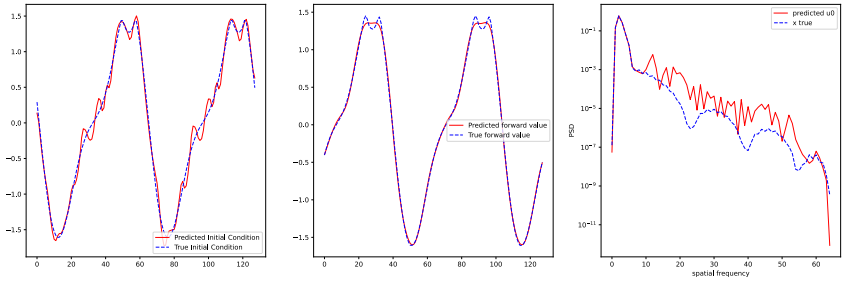

Figure 9: Inverse problem for the 1d advection equation with $\beta = 0.1$. The spectra density where most of the error is concentrated in the higher frequencies is depicted on the right.

D.10 Gradient-Based Inverse Method

The inverse problem aims at solving an inverse inference by minimising the prediction loss(Cao, 2018; Nocedal & Wright, 1999),

$$\mathcal{L}(u(t=T,x|u_0), u(t=T,x|\hat{u}_0))$$
$$\text{where} \quad \hat{u}_0 \sim p_\theta(u_0|u(t=T,x))\,.$$

The generation process $p_\theta(u_0|u(t=T,x))$ is a deterministic function, whose parameters θ use a bilinear interpolation to recover the initial condition (MacKinlay et al., 2021).

Figure 9 shows the solution of the inverse problem for the 1d advection equation. On the left, we see the true and estimated initial condition, and on the right the power density in the frequency domain. As we can see, the error is concentrated in the mid-high frequencies. In the middle we have the true and predicted value at time $t = T$. The error is smaller then in the plot on the left.

Table 1, Table 2 and Table 3 show the error in the spatial and frequency domain of 4 datasets and using FNO and U-Net as surrogate models. In Fig.9, the left figure visualizes the true and the estimated initial condition, while the middle figure is the predicted and the true value. As shown in the figure on the right, the largest error is in the higher frequencies. This effect is also visible from the frequency metrics of Tab.2 and Tab.3. In the experiment we use the same initial and boundary conditions of the forward problem.

E Detailed Baseline Score

F Detailed Runtime Comparison

In this section we present the detailed comparison of computation time between the PDE solver used to generate the data and the baseline models used in this work, summarized in Table 14. The system listed in Table 13 was used to run all timing measurements regarding the Diffusion-sorption, 2D diffusion-reaction and Shallow-water equation scenarios. PyClaw (Ketcheson et al., 2012), a well-optimized finite-volume Fortran code, is used as PDE solver for the shallow-water equation data generation. Note that the experiment is only running on a single core due to its small size. Because the PINN model is not discretized, the inference time includes evaluating the trained model at the same discretization points of the reference simulation for the last 20 time steps of the data. E.g. the

PDE	Metric	Forward model	
		FNO	U-Net
Advection_beta4	MSE	$2.4 \times 10^{-3} \pm 3.4 \times 10^{-3}$	$1.0 \times 10^{+0} \pm 5.6 \times 10^{-2}$
	nL2	$3.9 \times 10^{-2} \pm 2.9 \times 10^{-2}$	$1.0 \times 10^{+0} \pm 2.8 \times 10^{-2}$
	nL3	$4.4 \times 10^{-2} \pm 3.3 \times 10^{-2}$	$1.0 \times 10^{+0} \pm 2.9 \times 10^{-2}$
	MSE'	$2.9 \times 10^{-4} \pm 5.8 \times 10^{-4}$	$9.9 \times 10^{-1} \pm 2.5 \times 10^{-2}$
	nL2'	$1.4 \times 10^{-2} \pm 1.1 \times 10^{-2}$	$1.0 \times 10^{+0} \pm 8.0 \times 10^{-3}$
	nL3'	$1.6 \times 10^{-2} \pm 1.3 \times 10^{-2}$	$1.0 \times 10^{+0} \pm 8.4 \times 10^{-3}$
Burgers_Nu1	MSE	$1.0 \times 10^{+0} \pm 2.2 \times 10^{-1}$	$1.3 \times 10^{+0} \pm 2.3 \times 10^{-1}$
	nL2	$1.0 \times 10^{+0} \pm 1.0 \times 10^{-1}$	$1.1 \times 10^{+0} \pm 1.0 \times 10^{-1}$
	nL3	$1.0 \times 10^{+0} \pm 1.0 \times 10^{-1}$	$1.1 \times 10^{+0} \pm 1.1 \times 10^{-1}$
	MSE'	$1.3 \times 10^{-4} \pm 2.8 \times 10^{-4}$	$2.5 \times 10^{-3} \pm 1.9 \times 10^{-3}$
	nL2'	$7.0 \times 10^{-1} \pm 4.6 \times 10^{-1}$	$1.6 \times 10^{+1} \pm 2.0 \times 10^{+1}$
	nL3'	$7.0 \times 10^{-1} \pm 4.4 \times 10^{-1}$	$1.7 \times 10^{+1} \pm 2.1 \times 10^{+1}$
CFD_Shock_Trans	MSE	$3.4 \times 10^{+0} \pm 5.3 \times 10^{-1}$	$1.1 \times 10^{+2} \pm 2.0 \times 10^{+1}$
	nL2	$1.8 \times 10^{+0} \pm 1.4 \times 10^{-1}$	$1.0 \times 10^{+1} \pm 1.1 \times 10^{+0}$
	nL3	$1.9 \times 10^{+0} \pm 2.7 \times 10^{-1}$	$1.1 \times 10^{+1} \pm 1.6 \times 10^{+0}$
	MSE'	$1.0 \times 10^{-1} \pm 5.9 \times 10^{-2}$	$4.2 \times 10^{-1} \pm 9.2 \times 10^{-1}$
	nL2'	$3.3 \times 10^{-1} \pm 8.5 \times 10^{-2}$	$5.8 \times 10^{-1} \pm 3.9 \times 10^{-1}$
	nL3'	$3.6 \times 10^{-1} \pm 9.6 \times 10^{-2}$	$6.0 \times 10^{-1} \pm 4.0 \times 10^{-1}$
ReacDiff_Nu1_Rho2	MSE	$1.7 \times 10^{+0} \pm 2.1 \times 10^{-1}$	$2.0 \times 10^{+0} \pm 3.8 \times 10^{-1}$
	nL2	$1.3 \times 10^{+0} \pm 8.4 \times 10^{-2}$	$1.4 \times 10^{+0} \pm 1.3 \times 10^{-1}$
	nL3	$1.3 \times 10^{+0} \pm 8.1 \times 10^{-2}$	$1.5 \times 10^{+0} \pm 1.3 \times 10^{-1}$
	MSE'	$5.4 \times 10^{-2} \pm 1.2 \times 10^{-1}$	$6.4 \times 10^{-1} \pm 3.5 \times 10^{-1}$
	nL2'	$1.2 \times 10^{-1} \pm 1.2 \times 10^{-1}$	$7.3 \times 10^{-1} \pm 5.1 \times 10^{-2}$
	nL3'	$1.2 \times 10^{-1} \pm 1.2 \times 10^{-1}$	$7.3 \times 10^{-1} \pm 5.0 \times 10^{-2}$

Table 1: Error of the inverse problem. The prime indicates the error of the predition, for example MSE' is the MSE at time $t = T$. The MSE for example in the first row is one order of magnitude lower. nL2 and nL3 are the normalized L2 and L3 norm error, nLp = $||\hat{\boldsymbol{y}} - \boldsymbol{y}||_p / ||\boldsymbol{y}||_p, p = 2, 3$.

PDE	Metric	Forward model	
		FNO	U-Net
Advection_beta4	fMSE	3.04×10^{-1}	$1.29\times10^{+2}$
	fMSE low	5.56×10^{-1}	$1.29\times10^{+2}$
	fMSE mid	5.26×10^{-2}	$1.29\times10^{+2}$
	fMSE high	3.03×10^{-1}	$1.29\times10^{+2}$
	fMSE'	3.67×10^{-2}	9.92×10^{-1}
	fMSE' low	1.60×10^{-2}	9.92×10^{-1}
	fMSE' mid	5.74×10^{-2}	9.92×10^{-1}
	fMSE' high	3.68×10^{-2}	9.92×10^{-1}
	fL2	3.91×10^{-2}	$1.00\times10^{+0}$
	fL2 low	3.75×10^{-2}	$1.01\times10^{+0}$
	fL2 mid	$1.41\times10^{+1}$	$0.00\times10^{+0}$
	fL2 high	3.90×10^{-2}	$0.00\times10^{+0}$
Burgers_Nu1	fMSE	$1.29\times10^{+2}$	$1.59\times10^{+2}$
	fMSE low	$2.58\times10^{+2}$	$1.59\times10^{+2}$
	fMSE mid	1.19×10^{-1}	$1.59\times10^{+2}$
	fMSE high	$1.29\times10^{+2}$	$1.59\times10^{+2}$
	fMSE'	1.67×10^{-2}	2.46×10^{-3}
	fMSE' low	3.36×10^{-2}	2.46×10^{-3}
	fMSE' mid	9.26×10^{-7}	2.46×10^{-3}
	fMSE' high	1.66×10^{-2}	2.46×10^{-3}
	fL2	9.98×10^{-1}	$1.11\times10^{+0}$
	fL2 low	9.98×10^{-1}	$1.11\times10^{+0}$
	fL2 mid	$3.50\times10^{+0}$	$0.00\times10^{+0}$
	fL2 high	9.98×10^{-1}	$0.00\times10^{+0}$
CFD_Shock_Trans	fMSE	$4.37\times10^{+2}$	$1.40\times10^{+4}$
	fMSE low	$4.37\times10^{+2}$	$1.40\times10^{+4}$
	fMSE mid	$4.37\times10^{+2}$	$1.40\times10^{+4}$
	fMSE high	$4.37\times10^{+2}$	$1.40\times10^{+4}$
	fMSE'	$1.28\times10^{+1}$	$2.19\times10^{+2}$
	fMSE' low	$3.21\times10^{+1}$	$2.19\times10^{+2}$
	fMSE' mid	$1.13\times10^{+0}$	$2.19\times10^{+2}$
	fMSE' high	$8.98\times10^{+0}$	$2.19\times10^{+2}$
	fL2	$1.84\times10^{+0}$	$1.04\times10^{+1}$
	fL2 low	$1.51\times10^{+0}$	$9.95\times10^{+0}$
	fL2 mid	$0.00\times10^{+0}$	$0.00\times10^{+0}$
	fL2 high	$0.00\times10^{+0}$	$0.00\times10^{+0}$
ReacDiff_Nu1_Rho2	fMSE	$2.17\times10^{+2}$	$2.55\times10^{+2}$
	fMSE low	$6.10\times10^{+2}$	$2.55\times10^{+2}$
	fMSE mid	1.48×10^{-2}	$2.55\times10^{+2}$
	fMSE high	$1.28\times10^{+2}$	$2.55\times10^{+2}$
	fMSE'	$6.94\times10^{+0}$	6.35×10^{-1}
	fMSE' low	$2.77\times10^{+1}$	6.35×10^{-1}
	fMSE' mid	1.14×10^{-5}	6.35×10^{-1}
	fMSE' high	1.29×10^{-4}	6.35×10^{-1}
	fL2	$1.30\times10^{+0}$	$1.41\times10^{+0}$
	fL2 low	$1.54\times10^{+0}$	$1.60\times10^{+0}$
	fL2 mid	$7.45\times10^{+0}$	$0.00\times10^{+0}$
	fL2 high	$1.00\times10^{+0}$	$0.00\times10^{+0}$

Table 2: Frequency error of the inverse problem. fMSE, fL2 and fL3 are the frequency version of the MSE, normalized L2 and L3 norm metrics. Low, mid and high is the range of frequencies. Prime is used for the error in the prediction, without the error of the initial condition estimation. Normalised metric are not well defined, when the original signal is zero.

PDE	Metric	Forward model	
		FNO	U-Net
Advection_beta4	fL2'	1.36×10^{-2}	$1.13\times10^{+1}$
	fL2' low	7.50×10^{-3}	$5.66\times10^{+0}$
	fL2' mid	$1.61\times10^{+0}$	$5.27\times10^{+1}$
	fL2' high	1.36×10^{-2}	$8.01\times10^{+0}$
	fL3	3.14×10^{-2}	$1.00\times10^{+0}$
	fL3 low	3.12×10^{-2}	$1.00\times10^{+0}$
	fL3 mid	$1.75\times10^{+1}$	$0.00\times10^{+0}$
	fL3 high	3.14×10^{-2}	$0.00\times10^{+0}$
	fL3'	9.51×10^{-3}	$5.04\times10^{+0}$
	fL3' low	5.62×10^{-3}	$3.18\times10^{+0}$
	fL3' mid	$1.47\times10^{+0}$	$2.77\times10^{+1}$
	fL3' high	9.51×10^{-3}	$4.00\times10^{+0}$
Burgers_Nu1	fL2'	7.00×10^{-1}	$1.82\times10^{+2}$
	fL2' low	7.99×10^{-1}	$6.28\times10^{+1}$
	fL2' mid	$1.03\times10^{+2}$	$5.84\times10^{+5}$
	fL2' high	5.39×10^{-1}	$1.31\times10^{+2}$
	fL3	9.97×10^{-1}	$1.04\times10^{+0}$
	fL3 low	9.97×10^{-1}	$1.04\times10^{+0}$
	fL3 mid	$3.58\times10^{+0}$	$0.00\times10^{+0}$
	fL3 high	9.97×10^{-1}	$0.00\times10^{+0}$
	fL3'	7.21×10^{-1}	$4.88\times10^{+1}$
	fL3' low	7.99×10^{-1}	$2.40\times10^{+1}$
	fL3' mid	$9.35\times10^{+1}$	$2.98\times10^{+5}$
	fL3' high	5.39×10^{-1}	$3.92\times10^{+1}$
CFD_Shock_Trans	fL2'	3.34×10^{-1}	$2.12\times10^{+0}$
	fL2' low	2.68×10^{-1}	$2.14\times10^{+0}$
	fL2' mid	$0.00\times10^{+0}$	$0.00\times10^{+0}$
	fL2' high	$0.00\times10^{+0}$	$0.00\times10^{+0}$
	fL3	$1.26\times10^{+0}$	$9.41\times10^{+0}$
	fL3 low	$1.11\times10^{+0}$	$9.36\times10^{+0}$
	fL3 mid	$0.00\times10^{+0}$	$0.00\times10^{+0}$
	fL3 high	$0.00\times10^{+0}$	$0.00\times10^{+0}$
	fL3'	2.16×10^{-1}	$2.19\times10^{+0}$
	fL3' low	1.96×10^{-1}	$2.20\times10^{+0}$
	fL3' mid	$0.00\times10^{+0}$	$0.00\times10^{+0}$
	fL3' high	$0.00\times10^{+0}$	$0.00\times10^{+0}$
ReacDiff_Nu1_Rho2	fL2'	1.23×10^{-1}	$1.18\times10^{+1}$
	fL2' low	1.23×10^{-1}	$5.83\times10^{+0}$
	fL2' mid	$1.89\times10^{+18}$	$1.90\times10^{+21}$
	fL2' high	$9.03\times10^{+18}$	$3.93\times10^{+21}$
	fL3	$1.27\times10^{+0}$	$1.29\times10^{+0}$
	fL3 low	$1.45\times10^{+0}$	$1.47\times10^{+0}$
	fL3 mid	$7.07\times10^{+0}$	$0.00\times10^{+0}$
	fL3 high	$1.00\times10^{+0}$	$0.00\times10^{+0}$
	fL3'	1.23×10^{-1}	$5.08\times10^{+0}$
	fL3' low	1.23×10^{-1}	$3.18\times10^{+0}$
	fL3' mid	$1.07\times10^{+18}$	$7.25\times10^{+20}$
	fL3' high	$6.54\times10^{+18}$	$1.14\times10^{+21}$

Table 3: Frequency error of the prediction of the inverse problem. fMSE, fL2 and fL3 are the frequency version sof the MSE, normalized L2 and L3 norm metrics. Low, mid and high is the range of the frequencies. Prime is used for the error in the prediction, without the error of the initial condition estimation. Normalised metric are not well defined, when the original signal is zero.

Table 4: Summary of the baseline models' performance for different evaluation metrics: RMSE, normalised RMSE (nRMSE), RMSE from conserved value (cRMSE), maximum error, RMSE at the boundaries (bRMSE), RMSE in Fourier space at low (fRMSE low), medium (fRMSE mid), and high frequency (fRMSE high) ranges applied to the diffusion-sorption, 2D diffusion-reaction, and shallow-water equations.

PDE	Parameter	Metric	Baseline model		
			U-Net	FNO	PINN
Diffusion-sorption	N/A	RMSE	5.8×10^{-2}	5.9×10^{-4}	9.9×10^{-2}
		nRMSE	1.5×10^{-1}	1.7×10^{-3}	2.2×10^{-1}
		max error	2.9×10^{-1}	7.8×10^{-3}	2.2×10^{-1}
		cRMSE	4.8×10^{-2}	1.9×10^{-4}	7.5×10^{-2}
		bRMSE	6.1×10^{-3}	2.0×10^{-3}	1.4×10^{-1}
		fRMSE low	1.9×10^{-2}	1.5×10^{-4}	3.5×10^{-2}
		fRMSE mid	4.7×10^{-3}	5.0×10^{-5}	5.2×10^{-3}
		fRMSE high	1.9×10^{-4}	7.1×10^{-6}	2.7×10^{-4}
2D diffusion-reaction	N/A	RMSE	6.1×10^{-2}	8.1×10^{-3}	1.9×10^{-1}
		nRMSE	8.4×10^{-1}	1.2×10^{-1}	$1.6 \times 10^{+0}$
		max error	1.9×10^{-1}	9.1×10^{-2}	5.0×10^{-1}
		cRMSE	3.9×10^{-2}	1.7×10^{-3}	1.3×10^{-1}
		bRMSE	7.8×10^{-2}	2.7×10^{-2}	2.2×10^{-1}
		fRMSE low	1.7×10^{-2}	8.2×10^{-4}	5.7×10^{-2}
		fRMSE mid	5.4×10^{-3}	7.7×10^{-4}	1.3×10^{-2}
		fRMSE high	6.8×10^{-4}	4.1×10^{-4}	1.5×10^{-3}
Shallow-water equation	N/A	RMSE	8.6×10^{-2}	4.5×10^{-3}	1.7×10^{-2}
		nRMSE	8.3×10^{-2}	4.4×10^{-3}	1.7×10^{-2}
		max error	4.4×10^{-1}	4.5×10^{-2}	1.3×10^{-3}
		cRMSE	1.3×10^{-2}	2.0×10^{-4}	1.7×10^{-2}
		bRMSE	4.2×10^{-3}	1.4×10^{-3}	1.5×10^{-1}
		fRMSE low	2.0×10^{-2}	2.6×10^{-4}	5.9×10^{-3}
		fRMSE mid	7.0×10^{-3}	3.1×10^{-4}	1.9×10^{-3}
		fRMSE high	8.6×10^{-4}	2.5×10^{-4}	6.0×10^{-4}

2D diffusion-reaction scenario is evaluated at $128^2 \times 20$ discrete points. Additionally, autoregression is not required and therefore, it leads to significantly faster computation time relative to FNO and U-Net.

As the case for 3D data, we also performed a similar experiment whose results are summarized in Table 16. The used system information is listed in Table 15. Because of the severe memory usage, the resolution was reduced to 64^3, though we provided a data with resolution 128^3 in our official dataset. Note that the training and inference time are shorter than the 2D cases in Table 14. This is because the number of time-step and sample numbers are less than the 2D cases to reduce dataset size.

G Resolution Sensitivity of Inference Time

Figure 10 plots the resolution dependence of the inference time of classical simulation and ML methods for 2D/3D compressible Navier-Stokes equations cases. To calculate the inference times, we used the same hardware resources to be a "fair" comparison as listed in Table 15.

The figure clearly shows that the ML inference time is nearly 3-order of magnitude smaller than that of the classical simulations. Concerning the resolution dependence, both of the ML models show a similar dependence to the inviscid classical simulation method. Importantly, the inference time of ML models is in general independent of the diffusion coefficient, such as viscosity. On the other hand, the classical simulation methods increase their computation time with diffusion

Table 5: Summary of the baseline models' performance for different evaluation metrics: RMSE, normalised RMSE (nRMSE), RMSE from conserved value (cRMSE), maximum error, RMSE at the boundaries (bRMSE), RMSE in Fourier space at low (fRMSE low), medium (fRMSE mid), and high frequency (fRMSE high) ranges applied to the advection equation with different parameter values.

PDE	Parameter	Metric	Baseline model		
			U-Net	FNO	PINN
Advection	$\beta = 0.1$	RMSE	3.8×10^{-2}	4.9×10^{-3}	7.8×10^{-1}
		nRMSE	6.0×10^{-2}	9.3×10^{-3}	9.1×10^{-1}
		max error	4.9×10^{-1}	1.4×10^{-1}	$1.5 \times 10^{+0}$
		cRMSE	1.5×10^{-2}	5.0×10^{-4}	5.5×10^{-3}
		bRMSE	6.4×10^{-2}	4.3×10^{-3}	6.8×10^{-1}
		fRMSE low	1.2×10^{-2}	4.1×10^{-4}	1.8×10^{-1}
		fRMSE mid	5.6×10^{-3}	4.4×10^{-4}	4.9×10^{-4}
		fRMSE high	8.6×10^{-4}	2.9×10^{-4}	6.1×10^{-6}
	$\beta = 0.4$	RMSE	3.6×10^{-1}	5.9×10^{-3}	9.2×10^{-1}
		nRMSE	6.7×10^{-1}	1.1×10^{-2}	$1.1 \times 10^{+0}$
		max error	$1.7 \times 10^{+0}$	2.0×10^{-1}	$1.7 \times 10^{+0}$
		cRMSE	2.6×10^{-1}	4.6×10^{-4}	1.9×10^{-3}
		bRMSE	3.7×10^{-1}	5.5×10^{-3}	7.7×10^{-1}
		fRMSE low	1.3×10^{-1}	4.4×10^{-4}	2.1×10^{-1}
		fRMSE mid	2.3×10^{-2}	4.7×10^{-4}	3.4×10^{-3}
		fRMSE high	2.3×10^{-3}	3.4×10^{-4}	9.8×10^{-6}
	$\beta = 1.0$	RMSE	1.2×10^{-2}	3.5×10^{-3}	4.0×10^{-1}
		nRMSE	2.0×10^{-2}	5.9×10^{-3}	4.7×10^{-1}
		max error	1.7×10^{-1}	8.5×10^{-2}	7.6×10^{-1}
		cRMSE	6.6×10^{-3}	1.8×10^{-4}	6.0×10^{-3}
		bRMSE	3.0×10^{-2}	2.6×10^{-3}	3.0×10^{-1}
		fRMSE low	3.8×10^{-3}	1.7×10^{-4}	9.7×10^{-2}
		fRMSE mid	1.5×10^{-3}	2.1×10^{-4}	1.2×10^{-3}
		fRMSE high	4.3×10^{-4}	2.2×10^{-4}	2.2×10^{-5}
	$\beta = 4.0$	RMSE	1.6×10^{-2}	5.8×10^{-3}	6.6×10^{-1}
		nRMSE	2.6×10^{-2}	1.0×10^{-2}	7.7×10^{-1}
		max error	1.4×10^{-1}	1.1×10^{-1}	$1.0 \times 10^{+0}$
		cRMSE	8.1×10^{-3}	3.9×10^{-4}	2.0×10^{-2}
		bRMSE	3.0×10^{-2}	5.1×10^{-3}	5.5×10^{-1}
		fRMSE low	4.6×10^{-3}	4.9×10^{-4}	1.5×10^{-1}
		fRMSE mid	1.8×10^{-3}	5.7×10^{-4}	3.4×10^{-4}
		fRMSE high	4.7×10^{-4}	2.9×10^{-4}	1.5×10^{-5}

coefficient because of the stability condition, known as Courant-Friedrich-Lewy (CFL) condition, $\Delta t \propto \Delta x^2/\eta$ in the case of the explicit method. Here $\Delta x, \Delta t$ are time-step size and mesh size, respectively, and η is the diffusion coefficient. This is much severer restriction than the inviscid case whose CFL condition is $\Delta t \propto \Delta x$. Hence, we can conclude that ML methods could even be suitable for solving for the problem with including strong-diffusive regime.

H Error Comparison with PDE Solver

To further assess the benefit of the trained baseline models, we generated the 2D diffusion-reaction data using a PDE solver with higher resolution (512×512), and downsampled them to lower resolution (128×128). These downsampled data were assumed as the ground truth (low discretization error) and then were used to train the baseline models. The trained baseline model predictions were

Table 6: Summary of the baseline models' performance for different evaluation metrics: RMSE, normalised RMSE (nRMSE), RMSE from conserved value (cRMSE), maximum error, RMSE at the boundaries (bRMSE), RMSE in Fourier space at low (fRMSE low), medium (fRMSE mid), and high frequency (fRMSE high) ranges applied to the Burgers' equation with different parameter values.

PDE	Parameter	Metric	Baseline model		
			U-Net	FNO	PINN
Burgers'	$\nu = 0.001$	RMSE	1.1×10^{-1}	1.3×10^{-2}	5.3×10^{-1}
		nRMSE	3.4×10^{-1}	4.2×10^{-2}	9.6×10^{-1}
		max error	5.7×10^{-1}	2.8×10^{-1}	8.2×10^{-1}
		cRMSE	5.9×10^{-2}	8.5×10^{-4}	5.1×10^{-1}
		bRMSE	1.0×10^{-1}	9.3×10^{-3}	5.2×10^{-1}
		fRMSE low	4.1×10^{-2}	8.7×10^{-4}	1.6×10^{-1}
		fRMSE mid	1.1×10^{-2}	1.2×10^{-3}	1.3×10^{-2}
		fRMSE high	1.5×10^{-3}	7.7×10^{-4}	4.7×10^{-4}
	$\nu = 0.01$	RMSE	9.7×10^{-2}	6.4×10^{-3}	5.3×10^{-1}
		nRMSE	3.0×10^{-1}	2.0×10^{-2}	9.5×10^{-1}
		max error	5.4×10^{-1}	1.5×10^{-1}	7.5×10^{-1}
		cRMSE	4.0×10^{-2}	7.2×10^{-4}	4.7×10^{-1}
		bRMSE	9.7×10^{-2}	7.6×10^{-3}	4.8×10^{-1}
		fRMSE low	3.5×10^{-2}	7.8×10^{-4}	1.8×10^{-1}
		fRMSE mid	1.0×10^{-2}	9.6×10^{-4}	2.3×10^{-2}
		fRMSE high	9.6×10^{-4}	5.2×10^{-4}	1.2×10^{-3}
	$\nu = 0.1$	RMSE	7.5×10^{-2}	1.4×10^{-3}	4.9×10^{-1}
		nRMSE	2.8×10^{-1}	4.5×10^{-3}	8.8×10^{-1}
		max error	4.6×10^{-1}	3.0×10^{-2}	6.6×10^{-1}
		cRMSE	3.0×10^{-2}	4.5×10^{-4}	4.7×10^{-1}
		bRMSE	1.0×10^{-1}	2.5×10^{-3}	3.4×10^{-1}
		fRMSE low	2.9×10^{-2}	4.2×10^{-4}	1.5×10^{-1}
		fRMSE mid	5.6×10^{-3}	3.1×10^{-4}	1.0×10^{-2}
		fRMSE high	8.4×10^{-4}	5.4×10^{-5}	5.1×10^{-4}
	$\nu = 1.0$	RMSE	6.0×10^{-2}	8.1×10^{-4}	5.4×10^{-1}
		nRMSE	3.6×10^{-1}	3.1×10^{-3}	9.9×10^{-1}
		max error	3.9×10^{-1}	5.9×10^{-3}	7.1×10^{-1}
		cRMSE	6.4×10^{-2}	2.4×10^{-4}	5.3×10^{-1}
		bRMSE	6.6×10^{-2}	8.6×10^{-4}	6.1×10^{-1}
		fRMSE low	2.5×10^{-2}	3.2×10^{-4}	1.5×10^{-1}
		fRMSE mid	3.0×10^{-3}	2.4×10^{-5}	4.9×10^{-3}
		fRMSE high	5.9×10^{-4}	4.9×10^{-6}	2.6×10^{-4}

compared against data that were generated using the same PDE solver but with coarser resolution (higher discretization error). The error comparison is summarized in Table 17. We observed that generating the data with lower resolution already accumulates high discretization error, relative to the baseline model prediction error. However, further sensitivity analysis with regards to different resolutions is required in future works to determine if the resolution is fine enough to be assumed as the ground truth.

I Visualization of Model Predictions

In this section, we present visualizations of the baseline model predictions, compared against the generated datasets for the diffusion-sorption equation (Figure 11), 2D diffusion-reaction equation (Figure 12, Figure 13, and Figure 14), the shallow-water equation (Figure 15, Figure 16, and Fig-

Table 7: Summary of the baseline models' performance for different evaluation metrics: RMSE, normalised RMSE (nRMSE), RMSE from conserved value (cRMSE), maximum error, RMSE at the boundaries (bRMSE), RMSE in Fourier space at low (fRMSE low), medium (fRMSE mid), and high frequency (fRMSE high) ranges applied to the Darcy flow equation with different parameter values.

			Baseline model	
PDE	Parameter	Metric	U-Net	FNO
DarcyFlow	$\beta = 0.01$	RMSE	4.0×10^{-3}	8.0×10^{-3}
		nRMSE	$1.1 \times 10^{+0}$	$2.5 \times 10^{+0}$
		max error	6.8×10^{-2}	1.5×10^{-1}
		cRMSE	5.8×10^{-3}	1.3×10^{-2}
		bRMSE	6.3×10^{-4}	4.7×10^{-3}
		fRMSE low	2.5×10^{-3}	5.2×10^{-3}
		fRMSE mid	1.3×10^{-4}	1.5×10^{-4}
		fRMSE high	2.1×10^{-5}	1.6×10^{-5}
	$\beta = 0.1$	RMSE	4.8×10^{-3}	6.2×10^{-3}
		nRMSE	1.8×10^{-1}	2.2×10^{-1}
		max error	7.0×10^{-2}	8.9×10^{-2}
		cRMSE	6.0×10^{-3}	7.7×10^{-3}
		bRMSE	8.6×10^{-4}	5.0×10^{-3}
		fRMSE low	2.6×10^{-3}	3.6×10^{-3}
		fRMSE mid	1.9×10^{-4}	2.6×10^{-4}
		fRMSE high	4.4×10^{-5}	4.5×10^{-5}
	$\beta = 1.0$	RMSE	6.4×10^{-3}	1.2×10^{-2}
		nRMSE	3.3×10^{-2}	6.4×10^{-2}
		max error	9.0×10^{-2}	1.1×10^{-1}
		cRMSE	6.0×10^{-3}	1.1×10^{-2}
		bRMSE	3.5×10^{-3}	5.5×10^{-3}
		fRMSE low	3.0×10^{-3}	5.2×10^{-3}
		fRMSE mid	3.4×10^{-4}	5.1×10^{-4}
		fRMSE high	1.3×10^{-4}	1.5×10^{-4}
	$\beta = 10.0$	RMSE	1.4×10^{-2}	2.1×10^{-2}
		nRMSE	8.2×10^{-3}	1.2×10^{-2}
		max error	2.4×10^{-1}	3.2×10^{-1}
		cRMSE	9.9×10^{-3}	1.5×10^{-2}
		bRMSE	9.4×10^{-3}	1.6×10^{-2}
		fRMSE low	5.8×10^{-3}	8.3×10^{-3}
		fRMSE mid	9.8×10^{-4}	1.3×10^{-3}
		fRMSE high	3.6×10^{-4}	5.7×10^{-4}
	$\beta = 100.0$	RMSE	7.3×10^{-2}	1.1×10^{-1}
		nRMSE	4.4×10^{-3}	6.4×10^{-3}
		max error	$1.7 \times 10^{+0}$	$2.1 \times 10^{+0}$
		cRMSE	5.1×10^{-2}	8.9×10^{-2}
		bRMSE	4.6×10^{-2}	7.9×10^{-2}
		fRMSE low	2.9×10^{-2}	4.6×10^{-2}
		fRMSE mid	5.3×10^{-3}	7.6×10^{-3}
		fRMSE high	2.5×10^{-3}	3.6×10^{-3}

ure 17), 1D Advection equation Figure 18, 1D Burgers equation Figure 19, 1D Reaction-Diffusion equation Figure 20, 1D compressible NS equations Figure 21, 2D Darcy flow Figure 22, and 2D compressible NS equations Figure 23.

Table 8: Summary of the baseline models' performance for different evaluation metrics: RMSE, normalised RMSE (nRMSE), RMSE from conserved value (cRMSE), maximum error, RMSE at the boundaries (bRMSE), RMSE in Fourier space at low (fRMSE low), medium (fRMSE mid), and high frequency (fRMSE high) ranges applied to the 1d diffusion-reaction equation with different parameter values.

PDE	Parameter	Metric	Baseline model		
			U-Net	FNO	PINN
ReacDiff	$\nu = 0.5, \rho = 1.0$	RMSE	3.1×10^{-3}	6.3×10^{-4}	4.5×10^{-2}
		nRMSE	6.0×10^{-3}	1.4×10^{-3}	8.0×10^{-2}
		max error	1.8×10^{-2}	8.7×10^{-3}	7.6×10^{-2}
		cRMSE	2.5×10^{-3}	1.3×10^{-3}	4.3×10^{-2}
		bRMSE	3.7×10^{-3}	6.7×10^{-4}	7.5×10^{-2}
		fRMSE low	1.1×10^{-3}	4.1×10^{-4}	1.4×10^{-2}
		fRMSE mid	1.8×10^{-4}	9.1×10^{-6}	2.4×10^{-4}
		fRMSE high	1.8×10^{-5}	1.7×10^{-6}	3.7×10^{-6}
	$\nu = 0.5, \rho = 10.0$	RMSE	6.2×10^{-8}	$0.0 \times 10^{+0}$	1.4×10^{-2}
		nRMSE	6.5×10^{-8}	$0.0 \times 10^{+0}$	1.4×10^{-2}
		max error	6.2×10^{-8}	$0.0 \times 10^{+0}$	2.6×10^{-2}
		cRMSE	6.2×10^{-8}	$0.0 \times 10^{+0}$	6.2×10^{-3}
		bRMSE	6.2×10^{-8}	$0.0 \times 10^{+0}$	2.3×10^{-2}
		fRMSE low	1.6×10^{-8}	$0.0 \times 10^{+0}$	4.3×10^{-3}
		fRMSE mid	$0.0 \times 10^{+0}$	$0.0 \times 10^{+0}$	2.5×10^{-4}
		fRMSE high	$0.0 \times 10^{+0}$	$0.0 \times 10^{+0}$	2.9×10^{-6}
	$\nu = 2.0, \rho = 1.0$	RMSE	2.3×10^{-3}	2.9×10^{-4}	3.9×10^{-1}
		nRMSE	4.5×10^{-3}	7.0×10^{-4}	7.3×10^{-1}
		max error	2.0×10^{-2}	4.2×10^{-3}	3.9×10^{-1}
		cRMSE	1.9×10^{-3}	6.4×10^{-4}	3.9×10^{-1}
		bRMSE	1.8×10^{-3}	4.1×10^{-4}	3.9×10^{-1}
		fRMSE low	7.7×10^{-4}	1.9×10^{-4}	9.7×10^{-2}
		fRMSE mid	1.7×10^{-4}	9.2×10^{-6}	6.2×10^{-5}
		fRMSE high	2.6×10^{-5}	1.8×10^{-6}	3.4×10^{-6}
	$\nu = 2.0, \rho = 10.0$	RMSE	3.1×10^{-8}	6.2×10^{-8}	3.2×10^{-2}
		nRMSE	3.2×10^{-8}	6.5×10^{-8}	3.3×10^{-2}
		max error	3.1×10^{-8}	6.2×10^{-8}	3.2×10^{-2}
		cRMSE	3.1×10^{-8}	6.2×10^{-8}	3.2×10^{-2}
		bRMSE	3.1×10^{-8}	6.2×10^{-8}	3.1×10^{-2}
		fRMSE low	7.8×10^{-9}	1.6×10^{-8}	8.0×10^{-3}
		fRMSE mid	$0.0 \times 10^{+0}$	$0.0 \times 10^{+0}$	6.4×10^{-6}
		fRMSE high	$0.0 \times 10^{+0}$	$0.0 \times 10^{+0}$	2.7×10^{-7}

J VISUALIZATION OF INITIAL CONDITIONS

In this section, we provide a collection of initial condition visualizations for each problem. Figure 24 shows different radius of the initial perturbation used as the initial condition for five different samples of the 2D shallow-water equation data. Figure 25 shows different random uniform initial condition used for five different samples of the 1D diffusion-sorption equation data. Figure 26 shows different random noise used as the initial condition for five different samples of the 2D diffusion-reaction equation data.

In Figure 27, we plotted the several samples of the initial condition for 1D Advection and Burgers equations. Figure 28 is also the similar plot of the initial condition for 1D Diffusion-Reaction equation. Note that in this case the value of the scalar function is limited between 0 to 1 because of

Table 9: Summary of the baseline models' performance for different evaluation metrics: RMSE, normalised RMSE (nRMSE), RMSE from conserved value (cRMSE), maximum error, RMSE at the boundaries (bRMSE), RMSE in Fourier space at low (fRMSE low), medium (fRMSE mid), and high frequency (fRMSE high) ranges applied to the 1d compressible Navier-Stokes equation with different parameter values.

			Baseline model	
PDE	Parameter	Metric	U-Net	FNO
1DCFD	$\eta = \zeta = 0.01$ Rand periodic	RMSE	9.9×10^{-1}	2.7×10^{-1}
		nRMSE	3.6×10^{-1}	9.5×10^{-2}
		max error	$7.8 \times 10^{+0}$	$4.1 \times 10^{+0}$
		cRMSE	3.6×10^{-1}	5.0×10^{-2}
		bRMSE	$1.0 \times 10^{+0}$	2.2×10^{-1}
		fRMSE low	3.6×10^{-1}	7.3×10^{-2}
		fRMSE mid	1.2×10^{-1}	5.5×10^{-2}
		fRMSE high	9.2×10^{-3}	3.7×10^{-3}
	$\eta = \zeta = 0.1$ Rand periodic	RMSE	6.6×10^{-1}	9.3×10^{-2}
		nRMSE	7.2×10^{-1}	6.8×10^{-2}
		max error	$5.3 \times 10^{+0}$	$1.5 \times 10^{+0}$
		cRMSE	3.5×10^{-1}	2.7×10^{-2}
		bRMSE	6.8×10^{-1}	7.6×10^{-2}
		fRMSE low	2.5×10^{-1}	2.8×10^{-2}
		fRMSE mid	5.7×10^{-2}	1.3×10^{-2}
		fRMSE high	7.7×10^{-3}	2.0×10^{-3}
	inviscid Rand periodic	RMSE	$1.7 \times 10^{+1}$	4.7×10^{-1}
		nRMSE	$1.1 \times 10^{+0}$	1.2×10^{-1}
		max error	$2.0 \times 10^{+1}$	$7.1 \times 10^{+0}$
		cRMSE	$1.7 \times 10^{+1}$	6.7×10^{-2}
		bRMSE	$1.6 \times 10^{+1}$	3.5×10^{-1}
		fRMSE low	5.3×10^{-1}	$4.5 \times 10^{+0}$
		fRMSE mid	1.9×10^{-1}	1.6×10^{-1}
		fRMSE high	2.1×10^{-2}	2.6×10^{-3}
	inviscid Rand Outgoing	RMSE	$1.6 \times 10^{+0}$	2.6×10^{-1}
		nRMSE	$1.1 \times 10^{+1}$	$6.7 \times 10^{+0}$
		max error	$1.2 \times 10^{+1}$	$4.3 \times 10^{+0}$
		cRMSE	$1.5 \times 10^{+0}$	1.5×10^{-1}
		bRMSE	$1.8 \times 10^{+0}$	3.6×10^{-1}
		fRMSE low	6.8×10^{-1}	9.0×10^{-2}
		fRMSE mid	1.2×10^{-1}	4.5×10^{-2}
		fRMSE high	1.6×10^{-2}	6.7×10^{-3}
	inviscid Shock Outgoing	RMSE	4.1×10^{-1}	1.6×10^{-1}
		nRMSE	1.7×10^{-1}	4.7×10^{-2}
		max error	$6.6 \times 10^{+0}$	$3.8 \times 10^{+0}$
		cRMSE	2.1×10^{-1}	5.3×10^{-2}
		bRMSE	5.6×10^{-1}	2.4×10^{-1}
		fRMSE low	1.4×10^{-1}	3.7×10^{-2}
		fRMSE mid	5.3×10^{-2}	2.6×10^{-2}
		fRMSE high	1.1×10^{-2}	6.7×10^{-3}

the form of the source term. Finally, we provided several samples of the 1D and 2D CFD cases in Figure 29 and Figure 30.

Table 10: Summary of the baseline models' performance for different evaluation metrics: RMSE, normalised RMSE (nRMSE), RMSE from conserved value (cRMSE), maximum error, RMSE at the boundaries (bRMSE), RMSE in Fourier space at low (fRMSE low), medium (fRMSE mid), and high frequency (fRMSE high) ranges applied to the 2d compressible Navier-Stokes equation with different parameter values (first part).

			Baseline model	
PDE	Parameter	Metric	U-Net	FNO
2DCFD	$M = 0.1$, inviscid Rand periodic	RMSE	4.0×10^{-1}	2.6×10^{-1}
		nRMSE	6.6×10^{-1}	2.8×10^{-1}
		max error	$5.1 \times 10^{+0}$	$4.2 \times 10^{+0}$
		cRMSE	1.5×10^{-1}	1.6×10^{-2}
		bRMSE	4.3×10^{-1}	2.6×10^{-1}
		fRMSE low	1.1×10^{-1}	4.5×10^{-2}
		fRMSE mid	4.8×10^{-2}	4.4×10^{-2}
		fRMSE high	1.7×10^{-2}	1.6×10^{-2}
	$M = 0.1, \eta = \zeta = 0.01$ Rand periodic	RMSE	9.1×10^{-2}	2.3×10^{-2}
		nRMSE	7.1×10^{-1}	1.7×10^{-1}
		max error	$1.1 \times 10^{+0}$	4.0×10^{-1}
		cRMSE	3.6×10^{-2}	5.3×10^{-3}
		bRMSE	1.1×10^{-1}	2.2×10^{-2}
		fRMSE low	2.7×10^{-2}	5.7×10^{-3}
		fRMSE mid	8.2×10^{-3}	2.7×10^{-3}
		fRMSE high	2.6×10^{-3}	6.3×10^{-4}
	$M = 0.1, \eta = \zeta = 0.1$ Rand periodic	RMSE	4.7×10^{-2}	4.9×10^{-3}
		nRMSE	$5.1 \times 10^{+0}$	3.6×10^{-1}
		max error	6.7×10^{-1}	8.7×10^{-2}
		cRMSE	3.2×10^{-2}	3.2×10^{-3}
		bRMSE	6.6×10^{-2}	4.3×10^{-3}
		fRMSE low	1.3×10^{-2}	1.4×10^{-3}
		fRMSE mid	4.2×10^{-3}	4.3×10^{-4}
		fRMSE high	2.2×10^{-3}	1.4×10^{-4}
	$M = 1.0$, inviscid Rand periodic	RMSE	$1.5 \times 10^{+0}$	$1.4 \times 10^{+0}$
		nRMSE	4.7×10^{-1}	3.5×10^{-1}
		max error	$1.6 \times 10^{+1}$	$1.6 \times 10^{+1}$
		cRMSE	4.8×10^{-1}	1.6×10^{-1}
		bRMSE	$1.5 \times 10^{+0}$	$1.3 \times 10^{+0}$
		fRMSE low	4.8×10^{-1}	4.0×10^{-1}
		fRMSE mid	1.2×10^{-1}	1.2×10^{-1}
		fRMSE high	3.9×10^{-2}	3.9×10^{-2}

Table 11: Summary of the baseline models' performance for different evaluation metrics: RMSE, normalised RMSE (nRMSE), RMSE from conserved value (cRMSE), maximum error, RMSE at the boundaries (bRMSE), RMSE in Fourier space at low (fRMSE low), medium (fRMSE mid), and high frequency (fRMSE high) ranges applied to the 2d compressible Navier-Stokes equation with different parameter values (second part).

			Baseline model	
PDE	Parameter	Metric	U-Net	FNO
2DCFD	$M = 1.0, \eta = \zeta =$ 0.01 Rand periodic	RMSE	3.4×10^{-1}	1.2×10^{-1}
		nRMSE	3.6×10^{-1}	9.6×10^{-2}
		max error	$3.7 \times 10^{+0}$	$1.7 \times 10^{+0}$
		cRMSE	1.1×10^{-1}	1.8×10^{-2}
		bRMSE	3.6×10^{-1}	1.3×10^{-1}
		fRMSE low	1.1×10^{-1}	3.3×10^{-2}
		fRMSE mid	2.7×10^{-2}	1.5×10^{-2}
		fRMSE high	6.2×10^{-3}	3.6×10^{-3}
	$M = 1.0, \eta = \zeta = 0.1$ Rand periodic	RMSE	1.1×10^{-1}	1.5×10^{-2}
		nRMSE	9.2×10^{-1}	9.8×10^{-2}
		max error	$1.3 \times 10^{+0}$	2.4×10^{-1}
		cRMSE	4.8×10^{-2}	4.8×10^{-3}
		bRMSE	1.5×10^{-1}	1.7×10^{-2}
		fRMSE low	3.0×10^{-2}	3.2×10^{-3}
		fRMSE mid	1.3×10^{-2}	1.5×10^{-3}
		fRMSE high	4.3×10^{-3}	8.9×10^{-4}
	$M = 0.1$, inviscid Turb periodic	RMSE	3.3×10^{-1}	2.8×10^{-1}
		nRMSE	1.9×10^{-1}	1.6×10^{-1}
		max error	$2.2 \times 10^{+0}$	$1.8 \times 10^{+0}$
		cRMSE	1.5×10^{-2}	1.2×10^{-2}
		bRMSE	3.6×10^{-1}	2.8×10^{-1}
		fRMSE low	6.5×10^{-2}	5.0×10^{-2}
		fRMSE mid	3.2×10^{-2}	3.1×10^{-2}
		fRMSE high	8.5×10^{-3}	6.5×10^{-3}
	$M = 1.0$, inviscid Turb periodic	RMSE	9.5×10^{-2}	9.2×10^{-2}
		nRMSE	1.4×10^{-1}	1.3×10^{-1}
		max error	8.2×10^{-1}	7.9×10^{-1}
		cRMSE	6.5×10^{-3}	4.3×10^{-3}
		bRMSE	1.1×10^{-1}	9.7×10^{-1}
		fRMSE low	1.3×10^{-2}	1.1×10^{-2}
		fRMSE mid	1.2×10^{-2}	1.2×10^{-2}
		fRMSE high	5.2×10^{-3}	5.2×10^{-3}

Table 12: Summary of the baseline models' performance for different evaluation metrics: RMSE, normalised RMSE (nRMSE), RMSE from conserved value (cRMSE), maximum error, RMSE at the boundaries (bRMSE), RMSE in Fourier space at low (fRMSE low), medium (fRMSE mid), and high frequency (fRMSE high) ranges applied to the 3d compressible Navier-Stokes equation with different parameter values.

			Baseline model	
PDE	Parameter	Metric	U-Net	FNO
3DCFD	$M = 1.0$ inviscid Rand periodic	RMSE	$2.2 \times 10^{+0}$	6.0×10^{-1}
		nRMSE	$1.0 \times 10^{+0}$	3.7×10^{-1}
		max error	$9.0 \times 10^{+0}$	$3.6 \times 10^{+0}$
		cRMSE	$2.3 \times 10^{+0}$	8.1×10^{-2}
		bRMSE	$2.1 \times 10^{+0}$	6.0×10^{-1}
		fRMSE low	7.3×10^{-1}	1.1×10^{-1}
		fRMSE mid	7.6×10^{-2}	4.4×10^{-2}
		fRMSE high	2.3×10^{-2}	9.3×10^{-3}
	$M = 1.0$ inviscid Turb periodic	RMSE	8.1×10^{-2}	8.2×10^{-2}
		nRMSE	2.3×10^{-1}	2.4×10^{-1}
		max error	5.0×10^{-1}	4.5×10^{-1}
		cRMSE	7.3×10^{-3}	2.8×10^{-3}
		bRMSE	9.9×10^{-2}	8.6×10^{-2}
		fRMSE low	1.1×10^{-2}	7.2×10^{-3}
		fRMSE mid	8.0×10^{-3}	9.4×10^{-3}
		fRMSE high	1.7×10^{-3}	4.5×10^{-3}

Table 13: System configuration 1

CPU	$2 \times$ AMD EPYC 7742
GPU	$1 \times$ NVIDIA Volta V100
Software	PyTorch@1.11, CUDA@11.3

Table 14: Comparison of computation time between the PDE solver used to generate a single data sample and single forward runs of FNO, U-Net, and PINN. Training time of the baseline models for one epoch are also presented in this table. The unit used for the time is seconds.

PDE	Resolution	Model	Training time ($\frac{\text{s}}{\text{epoch}}$)	Epochs	Inference time (s)
Diffusion-sorption	$1\,024^1$	PDE solver	–	–	59.83
		FNO	97.52	500	0.32
		U-Net	96.75	500	0.32
		PINN	0.011	15 000	0.0027
2D diffusion-reaction	128^2	PDE solver	–	–	2.21
		FNO	108.28	500	0.40
		U-Net	83.19	500	0.61
		PINN	0.022	100	0.0077
Shallow-water equation	128^2	PDE solver	–	–	0.62
		FNO	105.16	500	0.37
		U-Net	83.32	500	0.56
		PINN	0.041	15 000	0.00673

Table 15: System configuration 2

GPU	$1 \times$ NVIDIA GeForce RTX 3090
Software (ML methods)	PyTorch@1.11, CUDA@11.3
Software (simulations)	JAX@0.2.26, CUDA@11.3

Table 16: Comparison of computation time between the PDE solver used to generate a single data sample and single forward runs of FNO, U-Net. Training time of the baseline models for one epoch are also presented in this table. The unit used for the time is seconds.

PDE	Resolution	Model	Training time ($\frac{s}{epoch}$)	Epochs	Inference time (s)
3D CFD	64^3	PDE solver	–	–	60.07
		FNO	24.77	500	0.14
		U-Net	62.22	500	0.27

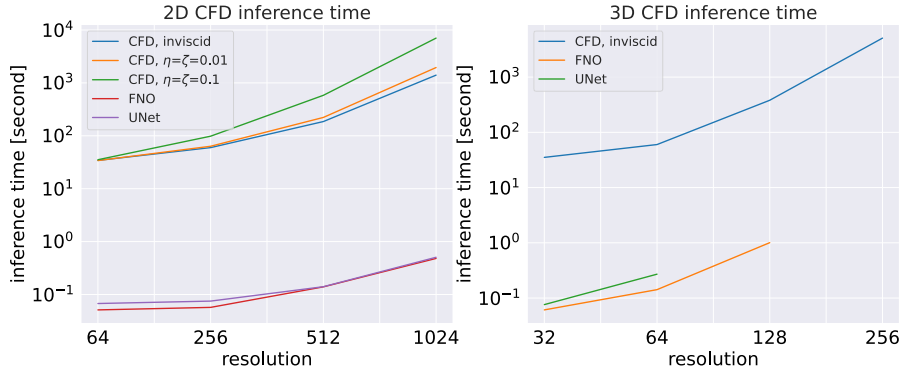

Figure 10: Plots inference time for 2D/3D CFD cases.

Table 17: Error comparison between of U-Net, FNO, and PINN prediction, as well as low-resolution PDE solver data, against the high-resolution PDE solver data (assumed as the ground truth) for the 2D diffusion-reaction scenario.

Error metric	U-Net	FNO	PINN	low-res PDE solver
RMSE	6.1×10^{-2}	8.1×10^{-3}	1.9×10^{-1}	1.8×10^{-1}
nRMSE	8.4×10^{-1}	1.2×10^{-1}	$1.6 \times 10^{+0}$	$2.8 \times 10^{+0}$
max error	1.9×10^{-1}	9.1×10^{-2}	5.0×10^{-1}	8.9×10^{-1}
cRMSE	3.9×10^{-2}	1.7×10^{-3}	1.3×10^{-1}	4.9×10^{-2}
bRMSE	7.8×10^{-2}	2.7×10^{-2}	2.2×10^{-1}	2.1×10^{-1}
fRMSE low	1.7×10^{-2}	8.2×10^{-4}	5.7×10^{-2}	4.9×10^{-2}
fRMSE mid	5.4×10^{-3}	7.7×10^{-4}	1.3×10^{-2}	2.2×10^{-2}
fRMSE high	6.8×10^{-4}	4.1×10^{-4}	1.5×10^{-3}	3.4×10^{-3}

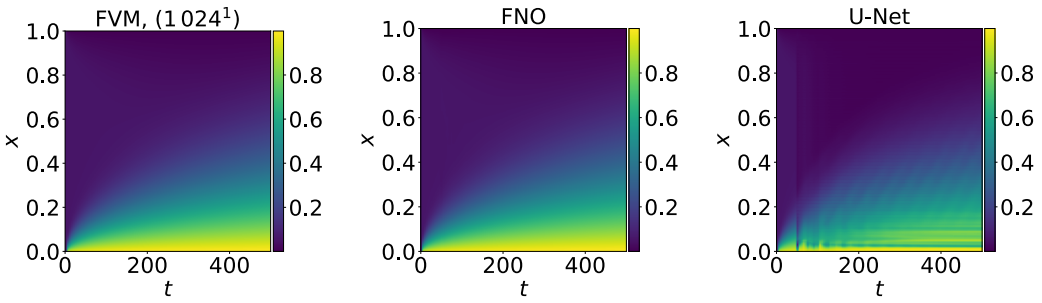

Figure 11: Visualization of the diffusion-sorption equation (a) data, (b) FNO prediction, and (c) U-Net prediction.

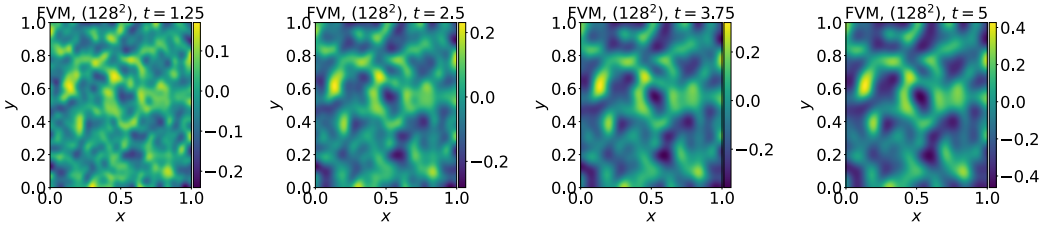

Figure 12: Visualization of the time evolution of the 2D diffusion-reaction equation data.

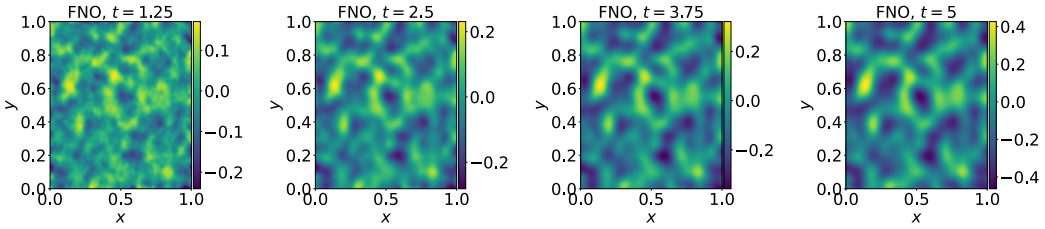

Figure 13: Visualization of the time evolution of the 2D diffusion-reaction equation predicted using FNO.

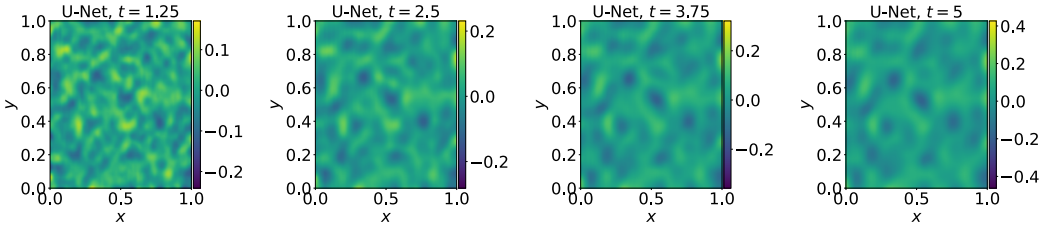

Figure 14: Visualization of the time evolution of the 2D diffusion-reaction equation predicted using U-Net.

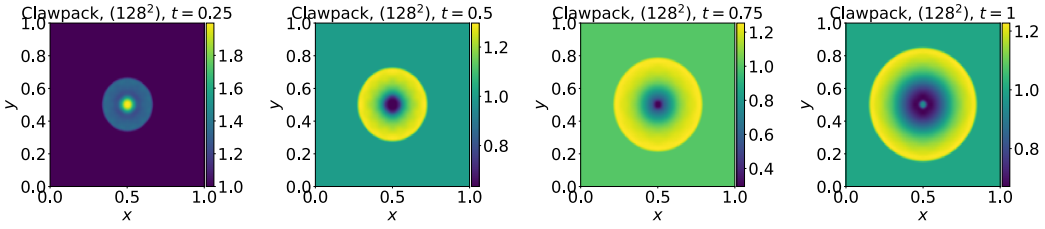

Figure 15: Visualization of the time evolution of the shallow water equation data.

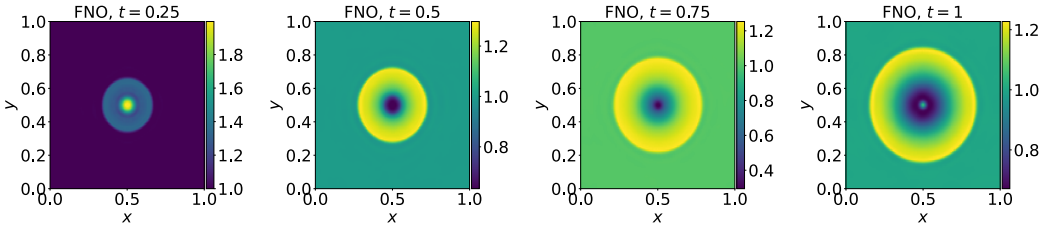

Figure 16: Visualization of the time evolution of the shallow water equation predicted using FNO.

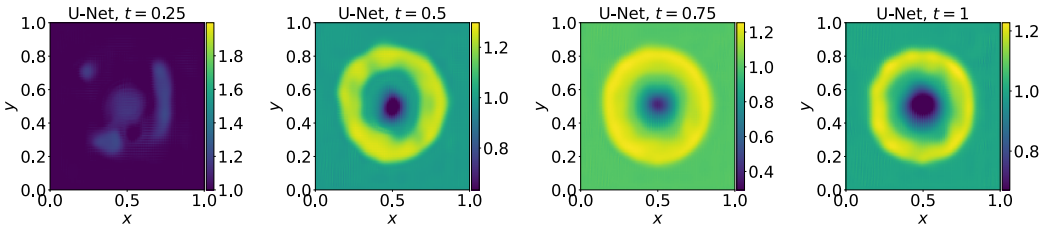

Figure 17: Visualization of the time evolution of the shallow water equation predicted using U-Net.

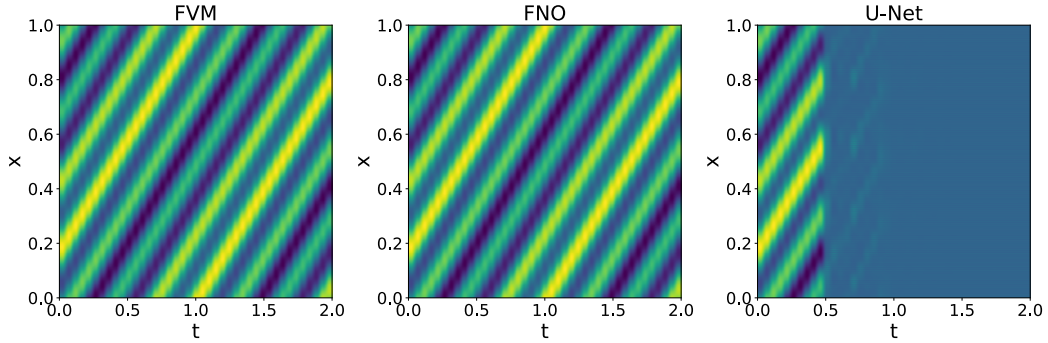

Figure 18: Plots of the predictions for 1D Advection equation.

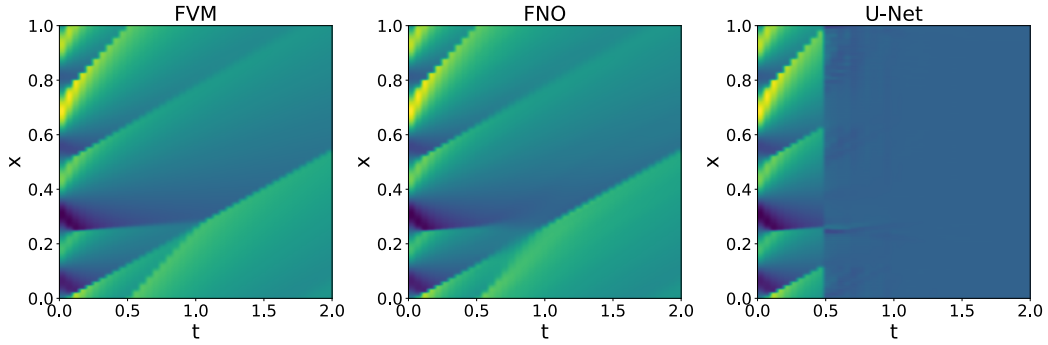

Figure 19: Plots of the predictions for 1D Burgers equation.

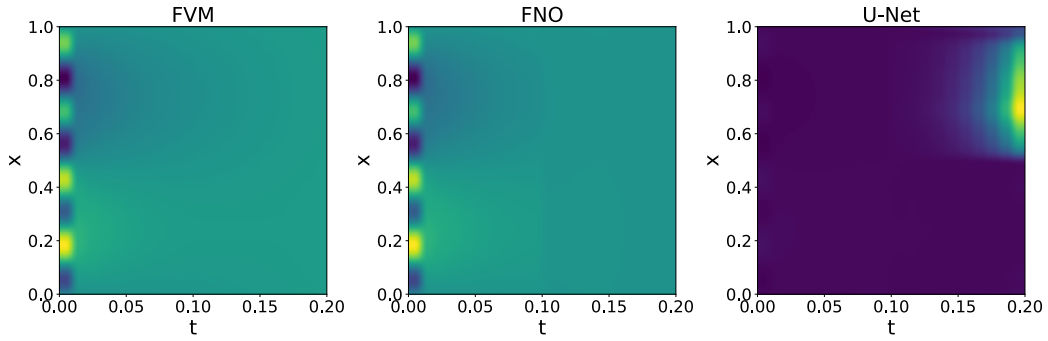

Figure 20: Plots of the predictions for 1D Reaction-Diffusion equation.

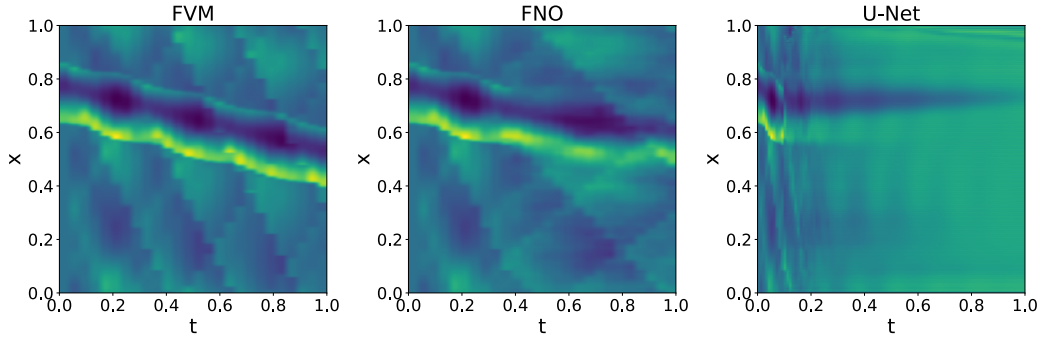

Figure 21: Plots of the predictions of density for 1D compressible NS equations.

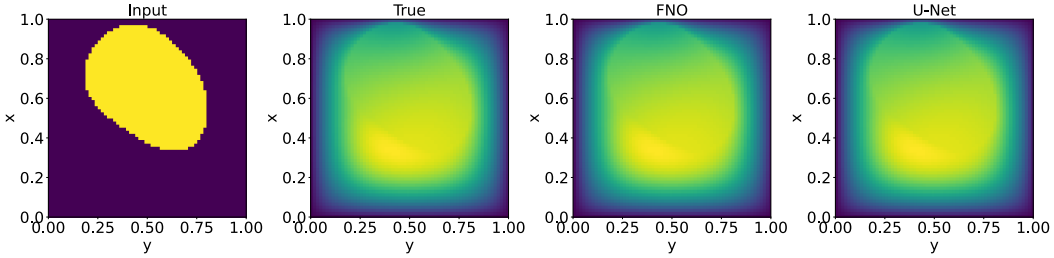

Figure 22: Plots of the predictions for 2D Darcy Flow.

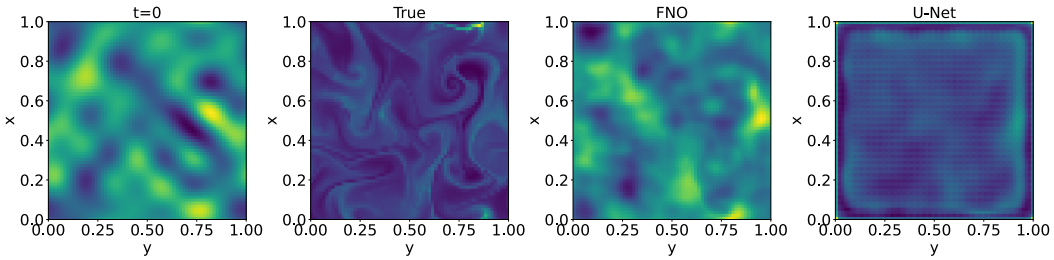

Figure 23: Plots of the predictions of the density for 2D compressible NS equations at the final time-step.

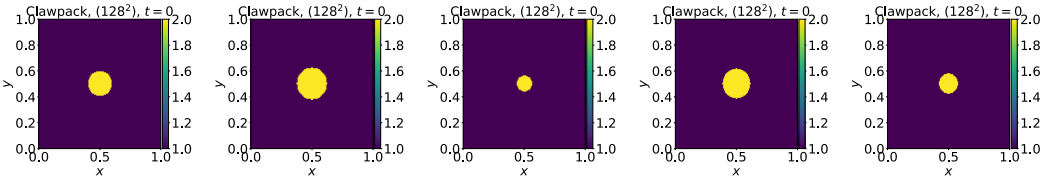

Figure 24: Visualization of the different radius of the initial perturbation used for the 2D shallow-water equations data.

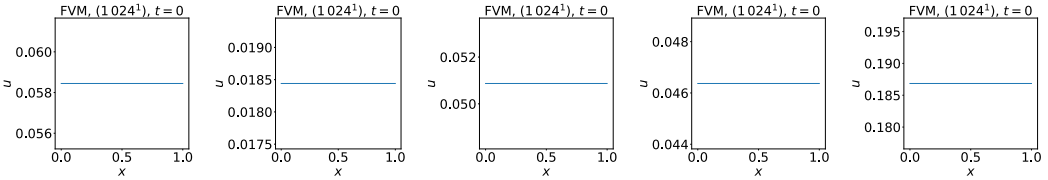

Figure 25: Visualization of the random uniform initial conditions used for the 1D diffusion-sorption equations data.

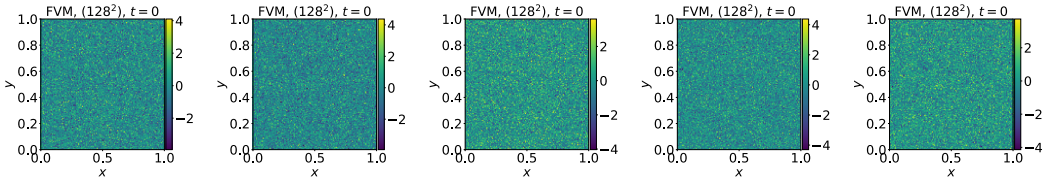

Figure 26: Visualization of the random initial conditions used for the 2D diffusion-reaction equations data.

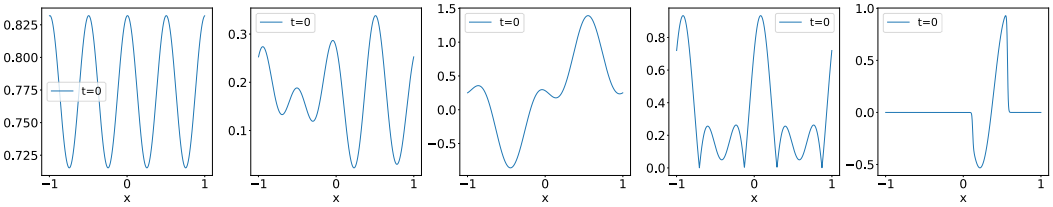

Figure 27: Visualization of the random initial conditions used for the 1D Advection/Burgers equations data.

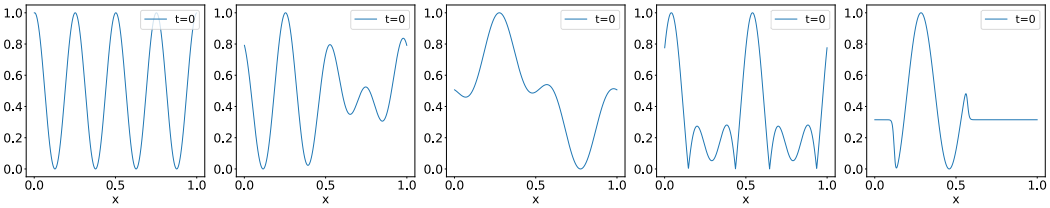

Figure 28: Visualization of the random initial conditions used for the 1D Reaction-Diffusion equations data.

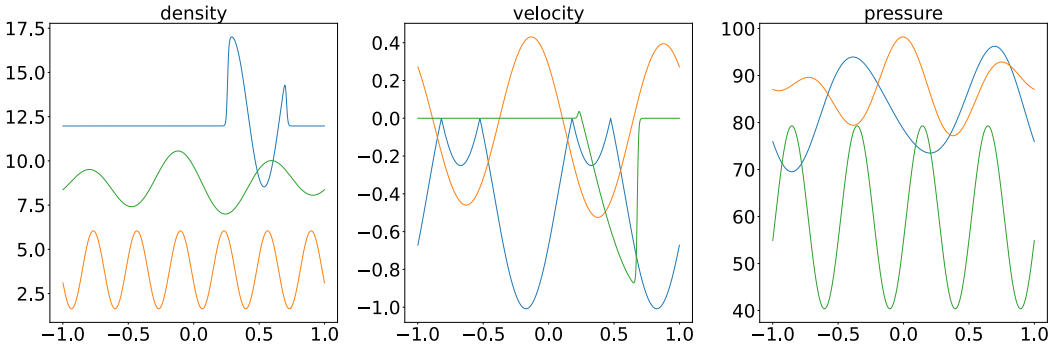

Figure 29: Visualization of the random initial conditions used for the 1D CFD data. The different colors mean the different samples.

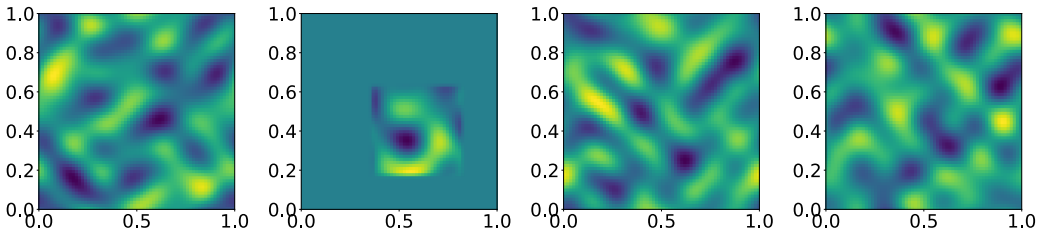

Figure 30: Visualization of the initial conditions of density used for the 2D CFD data.